Utrecht University

MASTER THESIS

Analysis of nontraditional Coriolis terms on linear equatorial shallow water model and boundary layers

Author:
Handi Liu

Supervisor:
Prof. J. da Silva
Prof. Leo R.M. Maas

Institute for Marine and Atmospheric research Utrecht (IMAU)

Utrecht University

May 2021

Abstract

The equatorial region is treated as a boundary layer in this study and analysed in numerical and analytical perspectives. A simple numerical equatorial dynamic model based on Zebiak and Cane's model (ZC model) is developed in this study. Though the model contains ocean-atmosphere coupled processes, it is found that the surface layer requires a more detailed description as a singularity occurs at the equator.

Dimensional analysis suggests that nontraditional Coriolis force terms and meridional diffusion terms are not negligible in the equatorial region. In consequence boundary layers occur both in meridional direction near the equator and in vertical direction, near the surface. Using matched asymptotic expansion, we conclude that the outer solutions of the problem follows parabolic characteristics. An attempt to find the inner solutions in both boundary layers (excluding overlapping region) is also presented in this study.

Through the discussion of these solutions, we show that the outer solutions originate from the surface boundary layer forced by surface wind stress in both hemispheres, develop in the form of parabolic characteristics, and converge at the equator through meridionally-oriented equatorial boundary layer. The equatorial boundary layer is a transition zone that connects both hemispheres, and the vertical structure within the equatorial boundary layer is related directly with the wind stress and the meridional pressure gradient at the surface in off-equator region.

Acknowledgments

I would first like to thank my supervisors Leo Maas and José da Silva for their valuable guidance and constant encouragement throughout the whole process of this project in every aspects. Their detailed feedback and advice with profession always inspired me after each meeting we had. I have learned from them not only the knowledge about this thesis topic, but more about the meaning of doing research.

Also, I would like to express my gratitude to Henk Dijkstra, whose valuable advice helped me in finding the information I needed. I would like to thank Haoy for helping me with the Fortran problems. The thanks also go to Kunyam Z. who provided technical support on programming when I tried almost every method and almost destroyed my laptop.

Next, I want to thank Emma, Julia, Luke, Lena, Miriam, Ruben and Sophie for the study hours we spent together, although I failed to attend the meetings many times. But it is a relief just knowing that you guys are also working hard and I am absolutely not alone, especially during the pandemic. I would like to thank my friends and family for supporting me even though we were separated in space (and in time). Last, I would like to thank Hanxuan for those wonderful stories and wisely quotes (though most of them were just daily conversations), reminding me of the beauty and poetry in one's life.

Contents

Chapter 1

Introduction

The dynamics in the equatorial regions is characterised by much smaller meridional and depth scales than mid-latitude regions and has many interesting phenomena. Owing to the small spatial scales, these phenomena are mostly confined to a narrow band centered at the equator. One of the most important properties in the equatorial region is the occurrence of Tropical Instability Waves (TIWs). The instability waves are travelling perturbations generated from strong velocity shear between the equatorial currents and equatorial counter currents, having a typical space scale of 1000-2000km and periods for 20-40 days (Willett et al., 2006). In figure 1.1 we can observe an example of TIWs in Pacific region. The cold tongue structure forms a narrow band centered at the equator, while at the south and north edges of the cold tongue, the perturbations propagate westward with a velocity of around 0.5 m/s, forming TIWs. We can also observe that TIW shapes the sea surface temperature (SST) fronts into cold cusps and warm troughs at the edge of the cold tongue. The TIWs are also found in Atlantic region, with similar properties (Caltabiano et al., 2005). TIWs are essential in determining the heat and momentum budget in the equatorial regions (Menkes et al., 2006), and they also influence the wind stress through TIW-induced SST anomalies, while the long-term SST value is affected via feedback process (Wei et al., 2019).

The indirect effects of TIW can be global, for example via the direct influence on instability of El Niño-Southern Oscillations (ENSO), one of the strongest climate fluctuations modes (Timmermann et al., 1999), and thus participating in the global climate system (Imada and Kimoto, 2012; Holmes et al., 2019), or via its influence of SST and mesoscale biology processes (Tian et al., 2019). However, the major dynamic phenomenon is confined within the narrow latitude band across the equator around $3°$S to $3°$N, where the cold tongue structure and the asymmetric ocean currents dominate.

In the same meridional range, unique phenomena are also observed in the deep ocean. In figure 1.2, we can observe the Equatorial Deep Jets (EDJs) that extend deep to 2 km in the ocean with periodical alternating zonal currents with the vertical wavelength of several hundred meters. In the Atlantic ocean, the EDJs are trapped within $1°$ in latitude according to both observations and model results from Eden

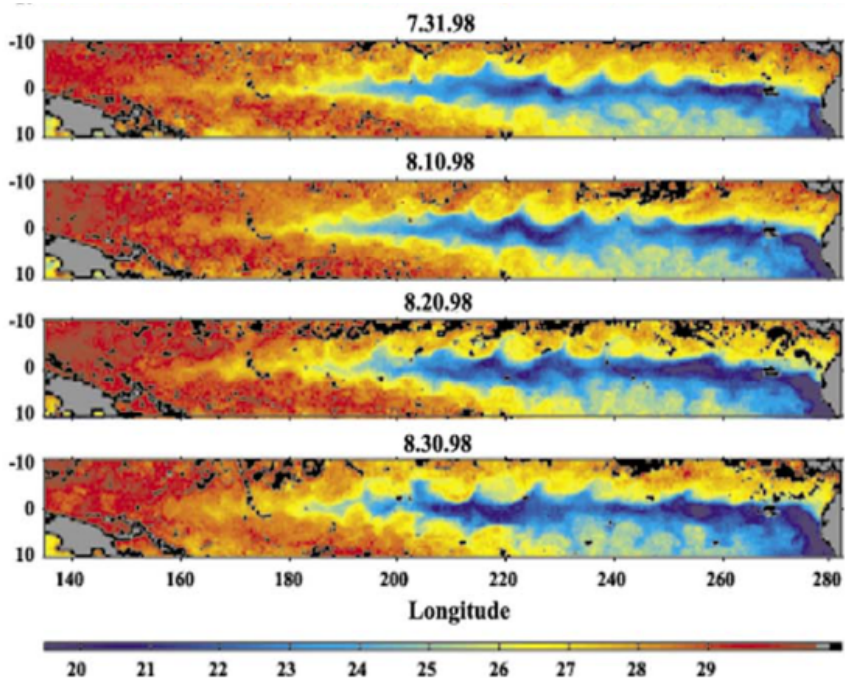

Figure 1.1: SST distribution derived from satellite data in the tropical Pacific (unit in $^{\circ}C$) from Willett et al. (2006). The numbers at the top of each panel indicate the time.

and Dengler (2008), who also promoted a mechanism that the EDJ are explained by Yanai and Kelvin waves produced by strong velocity shear at the equator, originating from western boundary currents. It has been found that the width of these deep jets are 1.5 times larger than expected from inviscid, linear theory and lateral eddy viscosity can explain the difference (Greatbatch et al., 2012). However, the forcing that causes the phase speed in vertical structure of EDJ is still not well explained.

One common feature of these phenomena is the limited meridional scale. This extremely small scale in meridional direction compared with the zonal scale of the ocean basin indicates that the dynamics is unique in this very thin layer in latitude and the equatorial regions may be viewed as a boundary layer which is located in meridional direction near the equator, similar to the classic Ekman theory (Ekman, 1905). Hence, the problem arises immediately: what role does this equatorial boundary layer play in the equatorial dynamics and can this concept improve our understanding of the horizontal or vertical structure of the equatorial ocean currents?

To answer these questions, we intend to first carry out a few series of numerical simulations as the background information of equatorial dynamics. The thermocline and SST gradient as well as the ocean currents are analysed in the simulations to obtain patterns of instability waves in the equatorial region. In the second part of the study, we will use analytical methods and analyse the boundary layer problem theoretically.

The thesis is structured as follows: we will introduce the modified numerical model in chapter 2 and discuss the numerical results in chapter 3. The discussion will lead

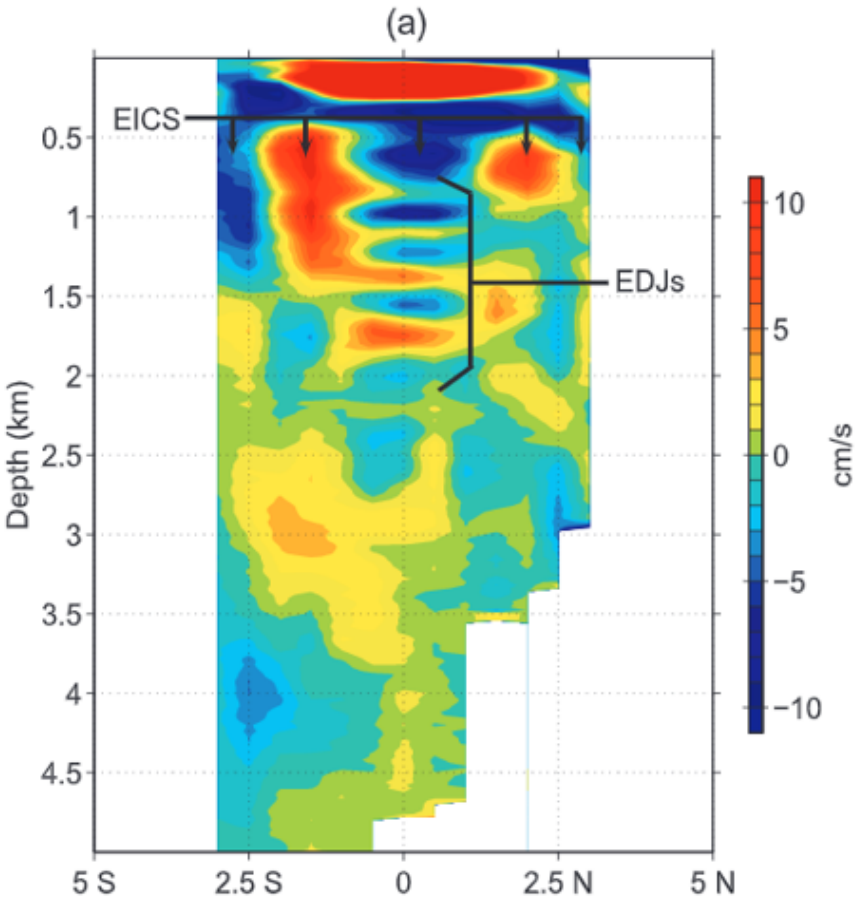

Figure 1.2: Zonal velocities at 159°W derived from observations in Line Island Profiling Project, reprinted from Ascani et al. (2010).

us to chapter 4 where analytical analysis on the boundary layer problem is presented. Finally, conclusions and outlook on future research are presented in chapter 5.

Chapter 2

Numerical Model

2.1 Governing Equations

2.1.1 Ocean Part

Following Zebiak and Cane (1987), we use 1.5-layer shallow water equations for ocean part, as described in equations (2.1) to (2.6), where subscripts of variables denote the corresponding partial derivatives:

$$u_{1,t} - \beta_0 y v_1 + g' h_x = \frac{\tau^x}{\rho h_1}, \tag{2.1}$$

$$v_{1,t} + \beta_0 y u_1 + g' h_y = \frac{\tau^y}{\rho h_1}, \tag{2.2}$$

$$u_{2,t} - \beta_0 y v_2 + g' h_x = 0, \tag{2.3}$$

$$v_{2,t} + \beta_0 y u_2 + g' h_y = 0, \tag{2.4}$$

$$h_{1,t} + (u_1 h_1)_x + (v_1 h_1)_y = 0, \tag{2.5}$$

$$h_{2,t} + (u_2 h_2)_x + (v_2 h_2)_y = 0. \tag{2.6}$$

The ocean basin is separated into a lower motionless layer II and an upper dynamic layer I based on the depth of thermocline, as shown in Figure 2.1. The thermocline depth h consists of two parts: the surface layer h_1 where the ocean is interacting with the atmosphere, and the underlying layer h_2. Both layers are controlled by momentum and continuity equations. The mean depths H, H_1 and H_2 are defined as the time-independent reference depths. The mean depths are used to deduce the geostrophic currents and provide a reference state in the SST equations discussed in following sections. Densities in both dynamic layer (ρ) and motionless layer ($\rho+\Delta\rho$) are constant. The reduced gravity is calculated from $g' = \frac{\Delta\rho}{\rho} g$. τ^x and τ^y are surface wind stress in zonal and meridional directions, influencing the surface layer. The equatorial beta-plane assumption is used with $\beta_0 = 2.2 \times 10^{-11}$ (ms)$^{-1}$.

Different from the original model, we are now considering the meridionally varying mean thermocline $H(y)$. Hence in continuity equations, instead of linear terms Hu_x and Hv_y, we have nonlinear terms $(uh)_x$ and $(vh)_y$. And meridional acceleration

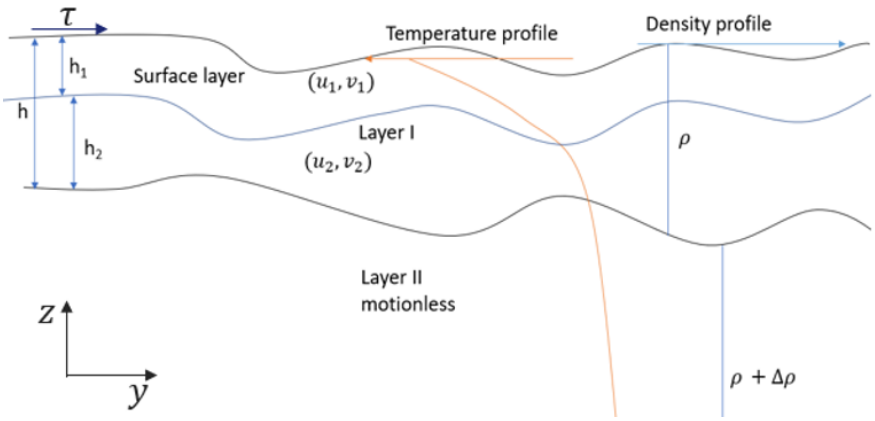

Figure 2.1: Sketch of the shallow water model. y is the meridional direction, and z is the vertical direction. The basin is separated into two major layers: one dynamic layer I and one motionless layer II. The temperature and density profiles are plotted for the purpose of explaining the occurrence of thermoclines and separation of the basin. In the dynamic layer, a thin surface mixing layer is added with the depth h_1.

terms are added to the momentum equations. The actual depths (h, h_1, h_2) are used in equations instead of their mean values.

The other model used in this study is modified from the Gmodel introduced by Burgers and van Oldenborgh (2003), whose governing equations are

$$u_t - \beta_0 y v + g' h_x = \frac{\tau^x}{\rho h}, \tag{2.7}$$

$$v_t + \beta_0 y u + g' h_y = \frac{\tau^y}{\rho h}, \tag{2.8}$$

$$h_t + (uh)_x + (vh)_y = Q. \tag{2.9}$$

Following the same procedure, we replace constant layer depth H in the equations with by varying $h(y)$, hence incorporating nonlinear terms $(uh)_x$ and $(vh)_y$. The original Gmodel does not include a mixed layer arguing that this provides more accurate surface velocities as suggested by observational results (Boulanger, 2001). In the original model, the forcing terms τ^x, τ^y and Q differ in the "forced" mode and the "coupled" mode. In the "forced" mode, τ^x and τ^y are retrieved from Florida State University (FSU) pseudo wind stress data and Q is zero, which means the model is composed of a dynamic ocean part and a static atmosphere part, though the SST is still changing via the SST equation (equation 2.16 in next section). In the "coupled" model, the interaction between atmosphere and ocean is provided by statistical regression using Nino-3 and Nino-4 indices. Hence, we need to modify also the atmosphere part of the Gmodel to formulate a physical interaction.

2.1.2 Atmosphere Part

For the ZC model, the governing equations for the atmospheric part are kept the same as in Gill's model (Gill, 1980) and consistent with that in Zebiak and Cane (1987). Here we provide a short description of the equations. The atmosphere is governed by horizontal velocities $\mathbf{u}_a = (u_a, v_a)$ and pressure p_a at the surface, satisfying

$$u_{a,t} - \beta_0 y v_a = -p_x, \tag{2.10}$$
$$v_{a,t} + \beta_0 y u_a = -p_y, \tag{2.11}$$
$$p_{a,t} + c_a^2 \nabla \cdot \mathbf{u}_a = -Q, \tag{2.12}$$

where c_a is the phase speed of an atmospheric Kelvin wave. In this study the situation where low heating rate is also investigated, hence stationary solutions with Rayleigh damping terms are considered. The equations (2.10)-(2.12) are simplified as:

$$\epsilon u_a - \beta_0 y v_a = -p_x, \tag{2.13}$$
$$\epsilon v_a + \beta_0 y u_a = -p_y, \tag{2.14}$$
$$\epsilon p + c_a^2 \nabla \cdot \mathbf{u}_a = -Q, \tag{2.15}$$

where ϵ is Rayleigh friction coefficient. The atmosphere model is then coupled with the ocean model through surface wind velocities and a heat forcing term Q, while Q is then separated into two parts $Q = Q_s + Q_l$. The first sensible heat (with subscript *s*) term is related to direct heat transmitted via variations in water vapour pressure Δe. This is related to the change in SST $\Delta T = T - T_0$ according to Clausius-Clapeyron equation

$$Q_s = \alpha \Delta e = \alpha \Delta T \frac{b}{T_0^2} \exp(-b/T_0) = \alpha_e \Delta T, \tag{2.16}$$

where α_e is the proportionality coefficient. The last latent heat (with subscript *l*) term is related to convergence of moisture. We use the same method as in the ZC model and evaluate this term through the convergence of surface wind:

$$Q_l = \beta(M(c + \bar{c}) - M(\bar{c})), \tag{2.17}$$

where $c = -\nabla \cdot \mathbf{u}_a$ is the convergence of surface wind, $\bar{c}$ denotes a prescribed mean value, and β is a constant coefficient. $M(x) = H(x)x$, where $H(x)$ is Heaviside function. The latent heat is considered only when moisture is brought into the area through a convergent wind field.

SST is evaluated by:

$$T_t + \alpha_T T + \frac{w_1}{H_1} H(w_1)(T - T_s(h)) + \mathbf{u}_1 \cdot \nabla T = 0, \tag{2.18}$$

where T_s is the subsurface temperature, which has the form of $T_s = T_1 \tanh(b_1 h_1) - \tanh(b_1 h_0)$, where h_1 is the actual mixing layer depth and h_0 is prescribed surface

layer depth, while in practice we take it as the mean depth $h_0 = H_1$. w_1 is the vertical velocity in the surface layer. This equation relates the derivation in SST with the upwelling of the ocean.

We kept the above Gill model as the dynamic atmospheric part of the Gmodel, whilst the SST evolution is described by equation (2.19), where α_1, α_2 and α_3 are longitude-dependent coefficients and $\tilde{h}$ is the difference of the thermocline depth $h(y)$ to its mean value $H(y)$ (Burgers and van Oldenborgh, 2003):

$$T_t = \alpha_1 \tilde{h} + \alpha_2 \tau^x + \alpha_3 T. \tag{2.19}$$

The result of SST equation (2.19) will be compared to that evaluated using (2.18), as well as to the "forced" mode.

2.2 Model Setup

2.2.1 Numeric Model Description

The numerical model uses the same setup as the Gmodel, though modifications are made to assemble the governing equations described previously. The model is built on a realistic rectangular basin extending from $123°$E to $69°$W and $29.5°$S to $29.5°$N, that covers an equatorial strip of the Pacific Ocean. This basin is discretized as $2° \times 1°$ (longitude$\times$latitude) grid points. Time steps are chosen $\Delta t = 28800$ s (8 hours) for the ocean model, and $\Delta t_a = 1152$ s (approximately 20 minutes) for the atmosphere model.

Variables are discretized in Arakawa C-grid type: depths (h, h_1, h_2, H, H_1, H_2) and SST (T) are evaluated at the center of a grid point, zonal velocities (u_1, u_2) are evaluated at the boundaries of a grid point that are normal to the x-axis, meridional velocities (v_1, v_2) are evaluated at the boundaries that are normal to the y-axis.

All ocean boundaries are chosen as no-slip boundaries, with conditions of no normal transport at boundaries.

2.2.2 Discretization of Equations

For the purpose of obtaining a stable result (either as steady state or non-divergent oscillation), we use a forward-backward in time and centered in space approach (Beckers, 1993) to discretize the equations in this study as this provides us with semi-implicit equations.

The spatial derivatives of variables are discretized as:

$$(\frac{\partial a}{\partial x_i})_j = \frac{a_{j+1} - a_{j-1}}{\Delta x_i}, \tag{2.20}$$

where $x_i \in \{x, y\}$, a is a target variable, j denotes the grid point number. The time derivatives are calculated according to the number of the current time step.

Taking the equations in the underlying layer as an example, after discretizing, equations (2.3), (2.4) and (2.6) become:

$$\begin{aligned}&\frac{h^{t+1}_{2,(i,j)} - h^{t}_{2,(i,j)}}{\Delta t} \\ &+ \frac{(u^t_{2,(i+\frac{1}{2},j)} + u^t_{2,(i+\frac{3}{2},j)})h^t_{2,(i+1,j)} - (u^t_{2,(i-\frac{1}{2},j)} + u^t_{2,(i-\frac{3}{2},j)})h^t_{2,(i-1,j)}}{4\Delta x} \\ &+ \frac{(v^t_{2,(i,j+\frac{1}{2})} + v^t_{2,(i,j+\frac{3}{2})})h^t_{2,(i,j+1)} - (v^t_{2,(i,j-\frac{1}{2})} + v^t_{2,(i,j-\frac{3}{2})})h^t_{2,(i,j-1)}}{4\Delta y} = 0,\end{aligned} \tag{2.21}$$

$$\frac{u^{t+1}_{2,(i+\frac{1}{2},j)} - u^t_{2,(i+\frac{1}{2},j)}}{\Delta t} - \beta_0 y_j \overline{v}^{t+s}_{2,(i+\frac{1}{2},j)} = -g' \frac{h^{t+1}_{(i+1,j)} - h^{t+1}_{(i,j)}}{\Delta x} + DA_u, \tag{2.22}$$

$$\frac{v^{t+1}_{2,(i,j+\frac{1}{2})} - v^t_{2,(i,j+\frac{1}{2})}}{\Delta t} + \beta_0 \overline{y}_{j+\frac{1}{2}} \overline{u}^{t+1-s}_{2,(i,j+\frac{1}{2})} = -g' \frac{h^{t+1}_{(i,j+1)} - h^{t+1}_{(i,j)}}{\Delta y} + DA_v, \tag{2.23}$$

with

$$s = \begin{cases} 0 & t = 2k \\ 1 & t = 2k+1 \end{cases}, k \in \mathbf{N}.$$

The Arakawa C-grid is already used in the above equations, with (i, j) denoting the ith grid in x direction and the jth grid in y direction. Variables with an overline represent the value at that specific grid point at which the variable is not evaluated according to C-grid type. The value is calculated by taking the average of two adjacent grid points. Superscripts denote the time step. s changes with each time step, thus changing the order of calculation and making the system semi-implicit. DA terms represent damping terms, which can be written as $DA_a = \gamma_1 a + \gamma_2 \nabla^2 a + \gamma_4 \nabla^4 a$, where $a \in \{u, v, h\}$.

The same approach is applied to the surface layer of the ocean model and the atmosphere dynamic model. For the SST equation, we use a forward in time and centred in space method. In Appendix A, a full set of discretized equations are presented.

2.2.3 Mean Thermocline Depth

As demonstrated in the previous sections, a prescribed thermocline depth is needed for both SST equations and atmospheric model. Using observed data (Chu and Fan, 2019) from expendable bathythermograph (XBT) and conductivity, temperature, depth (CTD) instruments. We calculated the zonal mean thermocline depth (H) (shown in Figure 2.2) using the data collected within our research area. As the data spreads over 57 years (1961-2017), the result only represents a long-term average thermocline depths which excludes influence from annual evolution and ENSO cycle. At $\pm 30°$, the thermocline depths become smaller with larger meridional gradient. Within the interval of $[-30°, -10°]$ the thermocline depths change

rapidly, increasing from 120 m to approximately 270 m. Similar behaviour exists in the northern hemisphere, except the interval of large gradient is narrower, limited within $[20°, 30°]$. Though the fitted curve suggests that the gradient becomes zero approaching the vicinity of 10°, observational data presents oscillations with an amplitude of about 21 m near the equator.

To simplify the problem, we first examine a symmetric shape of thermocline depth described by:

$$H(y) = \begin{cases} A_1 + b_1 \exp(-\frac{(y+30)^2}{2\sigma^2}) & y \leq -10 \\ A_2 + b_2 \cosh(\lambda y) & -10 < y \leq 0 \\ H(-y) & y > 0 \end{cases} . \tag{2.24}$$

Where y is the latitude in degrees, H is the thermocline in meters. The coefficients $A_1, A_2, b_1, b_2, \sigma, \lambda$ are chosen under the condition that $H(y)$ has continuous first order derivatives. The values are listed in table 2.1.

The mean surface layer depth H_1 is assumed to be constant as a first approximation. This is also the condition used in ZC model. However, as will be discussed later in chapter 4, this assumption needs to be considered more carefully.

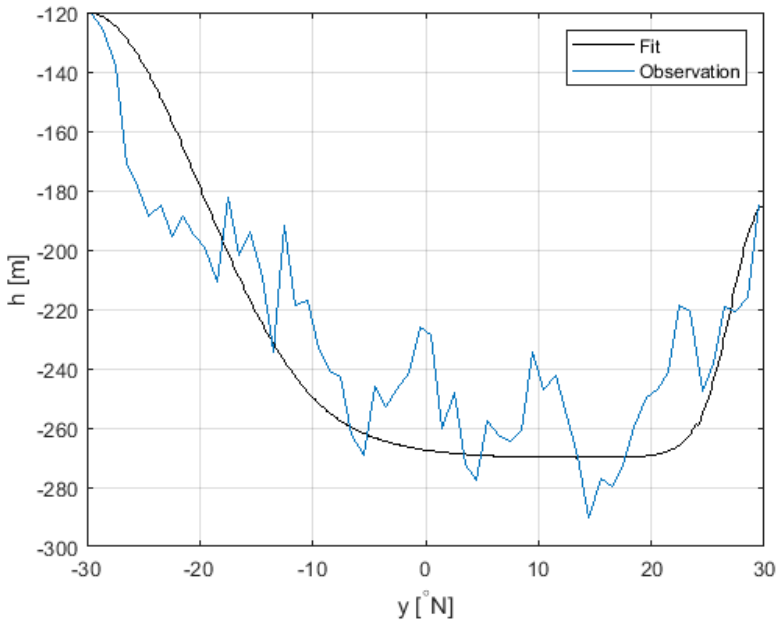

Figure 2.2: Zonal mean thermocline depth from observation data (blue) and fitted curve (black). The mean value is calculated within every 1° interval in latitude.

2.2.4 Model Parameter Values

The values for model parameters are listed in table 2.1.

Table 2.1: Description of parameters and their values.

Parameters	Description	Values (Units)
H_1	Thickness of mean surface layer	50(m)
Δx	Grid spacing in x-direction	2.22390$\times 10^5$(m)
Δy	Grid spacing in y-direction	1.11185$\times 10^5$(m)
Δt	Time step for ocean model	28800(s)
Δt_a	Time step for atmosphere model	1152(s)
g'	Reduced gravity	0.0323(m/s^2)
c_a	Atmospheric Kelvin wave phase speed	60(m/s)
β_0	Equatorial Rossby parameter	2.2$\times 10^{-11}$ (m^{-1}s^{-1})
(A_1, A_2)	Coefficient in zonal mean thermocline depth	(280,280) (m)
(b_1, b_2)	Coefficient in zonal mean thermocline depth	(-150,-5.066) (m)
ϵ	Rayleigh friction coefficient	0.5 (day^{-1})
σ	Coefficient in zonal mean thermocline depth	10 (degree)
λ	Coefficient in zonal mean thermocline depth	-0.2065 (degree^{-1})

2.3 Model discussion

Both numerical models (the ZC model and the Gmodel) aim to analyse the air-sea coupled dynamics within Pacific equatorial regions while the original Gmodel does not contain the dynamic descriptions for the atmosphere. We apply the Gill model to the Gmodel to provide the feedback process of the atmosphere, however the description for SST does not contain the moisture convergence which is relevant to the mixing layer. Hence we use the ZC model as a more realistic simulation of the physical processes.

In this study the density of the ocean is assumed to be constant in both models, while this may be violated when we consider the variation in SST. However, the dependence of the density on temperature is not a consideration in our study.

The time steps for the oceanic and atmospheric part are chosen in the way that the numerical model is stable, hence the Courant-Friedrichs-Lewy (CFL) condition must be satisfied by:

$$c\sqrt{2\left((\frac{\Delta t}{\Delta x})^2+(\frac{\Delta t}{\Delta y})^2\right)} \leq 1, \tag{2.25}$$

where $c=\sqrt{g'H}$ is the Kelvin wave speed, the left hand side is the CFL number for the numeric scheme discussed in section 2.2.2 (Beckers and Deleersnijder, 1993). To examine the actual behaviour of the numerical models, we use the concept of total energy (TE) in this study. The total energy of the basin at a given time step is calculated as the sum of the potential energy and the kinetic energy, represented by:

$$TE=\frac{1}{2}\iint_{\Omega} g(h-H)^2+h(u^2+v^2)dxdy \tag{2.26}$$

where Ω is the whole basin, h is the thermocline depth and H is the prescribed mean value for thermocline depth. The first term in the integration represents the potential energy at certain position. As we are considering the energy compared to a reference state, the mean depth $H(y)$ should also be considered in the calculation as it varies with latitude. The second term in the integration represent the kinetic energy at certain position. In practice, the TE averaged over the area Ω is used.

The numerical models in this study are built on idealistic ocean basin and do not include the realistic continental boundaries. Therefore, the results of the models can only illustrate the basic pattern of the equatorial dynamics, which can be interpreted as the idealised solutions that contains distortion. However, these solutions still provide information to the patterns of equatorial dynamics.

Chapter 3

Result and Discussion

In this study, three sets of numerical experiments are performed separately with the Gmodel (forced mode), Gmodel (coupled with Gill's model), and ZC model. As discussed above, the forced Gmodel does not include air-sea interaction and only has a SST equation. Hence, we may observe the dynamic behaviour of the ocean under a shallow water scheme forced by prescribed wind stress while the SST may evolve physically. Still, it can be interesting to see how well the empirical equation performs with thermocline gradients in this mode. In the second run, the Gmodel is coupled with Gill's model, thus containing a dynamic atmosphere part. While the Gill model is assumed to have small time variance, the coupled model may illustrate the behaviour of the system with a small heating rate. In the last run, we use the modified ZC model and intend to simulate the sea-air interaction with more specific physics processes by adding the mixing layer and dynamic atmosphere model. The numerical results are shown in the following sections

3.1 Gmodel (forced mode)

The Gmodel is initialized with the geostrophic currents derived from $H(y)$ and is forced by annually varying wind stress terms derived from FSU wind stress data of the year 1978. Since the reference state $H(y)$ has only meridional gradient, the geostrophic currents only have zonal components. While at the eastern and western boundaries, the geostrophic currents obviously do not satisfy the boundary conditions that the normal transport is zero. However, it is only used as the initial condition and we believe it will be automatically adjusted by the model through friction terms and boundary conditions. The total simulated time is 700 weeks, while the model becomes stable after about 200 weeks, as is shown in the total energy plot (Fig.3.1).

To the end of the run, the model is characterized by periodic behaviour having the same frequency as the wind forcing terms. This is expected since in the forced mode, interaction between ocean and atmosphere is simplified as a one-way influence from the atmosphere in the form of surface wind stress. Hence, the steady state of the ocean is only determined by surface wind stress under this model settings.

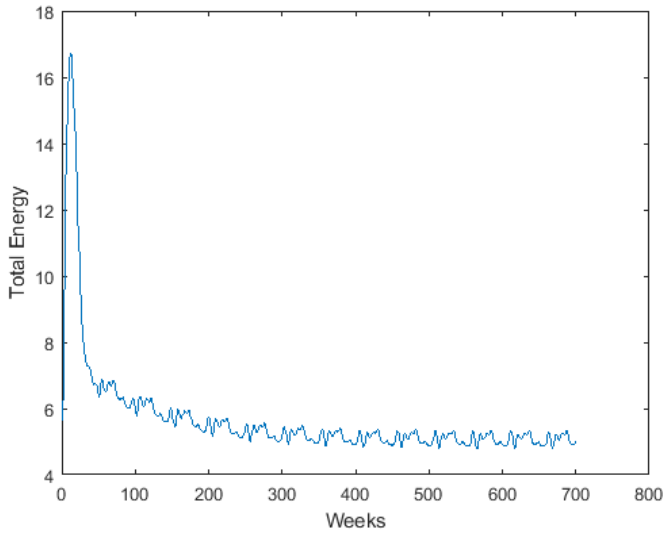

Figure 3.1: Total energy plot of forced Gmodel run. Vertical axis shows the total enery per cell of the basin, horizontal axis shows the simulated time in weeks.

As we are interested in the dynamics of equatorial regions, we then focus on a latitude band $[0°, 5°N]$ and examine the current velocities as well as the thermocline distributions. From the Hovmoller diagram of averaged zonal velocity (Fig.3.2) we can observe clearly the periodic variations that divide the diagram into four similar parts. Within each period, waves can be identified propagating both westward and eastward. The westward waves occur in the west part of the basin around $[123°E, 220°E]$, with average zonal velocity u smaller than 0.1 m/s. The phase speed of this westward wave is about 1.98 m/s, which we recognize as westward-propagating Rossby waves.

The eastward waves occur almost across the whole region, however waves with larger zonal velocities (u above 0.25 m/s) show different patterns. One set of these waves are faster waves located in the west part from $123°E$ to around $240°E$, indicated by the very first eastward wave starting from week 400. The phase speed of these waves is around 2.15 m/s. The other set of the waves are slower waves located from $180°E$ to the eastern boundary, indicated in Fig 3.2 by clusters of bright curves, e.g., major part in the Hovmoller diagram from week 410 to week 460. The speeds of this set of waves decays as they move from the west to the east. We recognize this set of waves as the equatorial Kelvin waves, whose speed is calculated as $c = \sqrt{g'h} \approx 1.96$ m/s. As can be observed in the Hovmoller diagram of thermocline depth (Fig.3.3a), the thermocline depth shows a decaying trend towards the east, hence explaining slower Kelvin wave speed towards the east.

Similar properties can also be observed in the diagram of the thermocline depth anomaly (Fig.3.3b). The periodic behaviour correspond to the annual wind stress. The waves discussed above can also be recognized in the diagram for h, though the clusters of easterly propagating waves seems to have disappeared since most of the eastern region has small h and makes the waves unapparent. It is interesting that

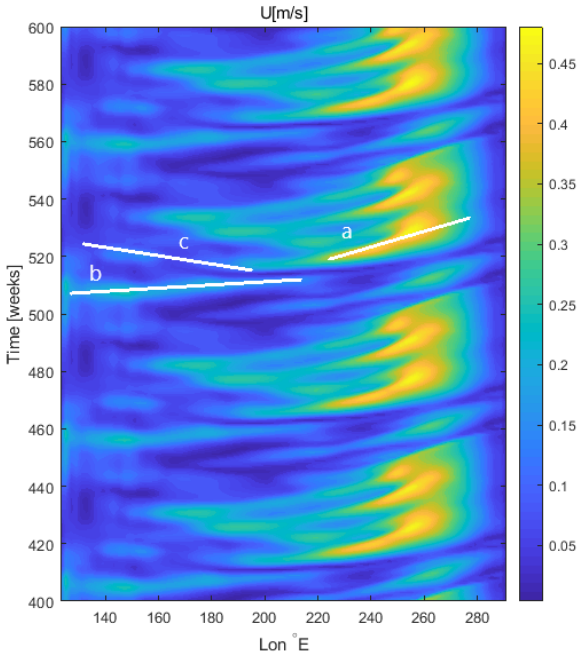

Figure 3.2: Hovmoller diagram of the zonal velocity u averaged in $[0°, 5°N]$, unit in m/s. Vertical axis indicates the simulated time in weeks, horizontal axis indicates the longitudes. White lines indicate instability waves: a) slow eastward propagating waves, b) faster eastward propagating waves, and c) westward propagating waves.

the thermocline depth drops to 20 m near the eastern boundary while the maximum value reaching 160 m is obtained at the western side.

The SST anomaly distribution at week 700, the end of the total simulation, is shown in Fig.3.4. The distribution of SST anomalies shows an asymmetric pattern, which is related to the realistic wind stress we are using. The SST shows strong negative anomalies in the whole region, except near the boundaries. The maximum positive anomaly is smaller than 0.5°C, while the negative anomaly exceeds 4°C. The SST anomalies are concentrated in the central Pacific. This may be explained by SST equation (2.19) where the second term representing the advection of zonal currents plays the dominant part in the central Pacific. However, the typical cold-tongue pattern is not obvious in the model run. This is expected since the feedback from the atmosphere is not included in the forced Gmodel and the wind forcing terms have a short period of one year.

3.2 Gmodel (coupled)

As the forced model does not contain the feedback from the atmosphere, it is not a proper model to analyse the realistic equatorial dynamics. We decide to take the dynamics of the atmosphere into account and build a coupled model. The coupled Gmodel uses the oceanic part of Gmodel and the Gill's model described by equations

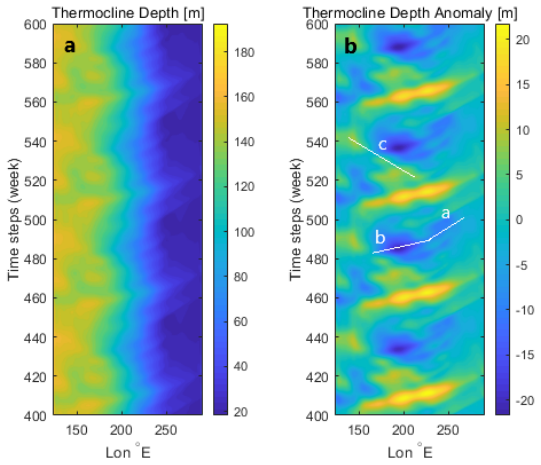

Figure 3.3: (a) Hovmoller diagram of the thermocline depth h averaged in $[0°, 5°N]$, unit in m. Vertical axis indicates the simulated time in weeks, horizontal axis indicates the longitudes. (b) Hovmoller diagram after subtracting the zonal trend (averaged from week 400 to week 600). The white lines a, b and c show the slow eastward propagating waves, fast eastward propagating waves and the westward propagating waves separately.

(2.13)-(2.15), along with a SST equation (2.19). The heat forcing only contains the sensible heat term as described in equation (2.16). The total energy plot is shown in Fig.3.5. In the first 100 weeks, the basin is forced by realistic wind stress terms, the same as in forced Gmodel. At the 100th week, the coupled model is activated and the wind stress is no longer prescribed but determined by the output of the atmospheric part. However, this coupled model does not show any sign of oscillations but tends to become steady toward the end of the simulation. As is shown by Fig.3.5, after about 50 weeks from the switching point, the total energy tends to decay exponentially and becomes a smooth curve afterwards. The zonal velocity diagram (Fig.3.6) and the SST anomaly diagram (Fig.3.7) also show the same result.

Clearly, after the transition from the forced mode to a coupled mode, the periodical oscillations disappear. Toward the end of the simulation, the basin shows a zonally homogeneous pattern indicated in both Hovmoller diagrams. Both velocity and SST anomaly converge to zeros after week 100 instead of the periodical oscillation as we observed in forced Gmodel. The slower eastward propagating wave discussed in last section still occurs in the velocity diagram shown by white line a. We believe this is caused by the abrupt transition that the dynamic atmosphere is added to the model. The wave with intensified zonal velocity dissipates after around 20 weeks when it reaches the east boundary. The westward propagating waves are also observed in Fig.3.6. In the SST diagram, the zonally noncontinuous behaviours still exist. This may be related to the SST equation (2.19), which separates the basin into different regions where different processes domains in each region, as shown by black lines in the figure. To the west of b_1 and to the east of b_3 the coefficient α_2 becomes zero, as the advection of zonal currents are only significant in the central Pacific. Around line b_2 ($190°E$ to $200°E$) an abrupt change of coeffcients α_1 and α_3 exist as a simulation

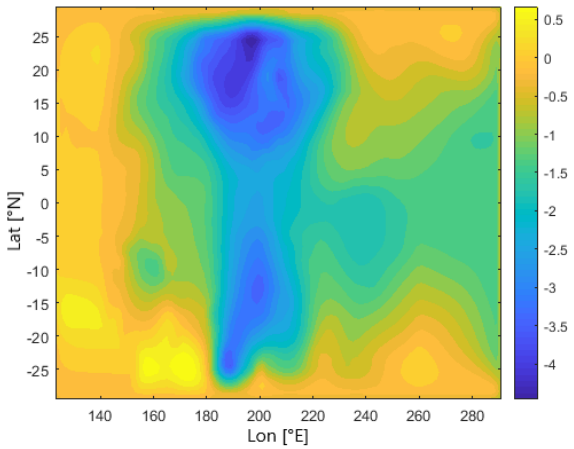

Figure 3.4: Contour plot of SST anomaly distribution at the end of the simulation, unit in K. The vertical axis shows the latitude ($^\circ N$), horizontal axis shows the longitude ($^\circ E$). Anomaly is calculated to the initial states where SST are assumed to be uniformly distributed.

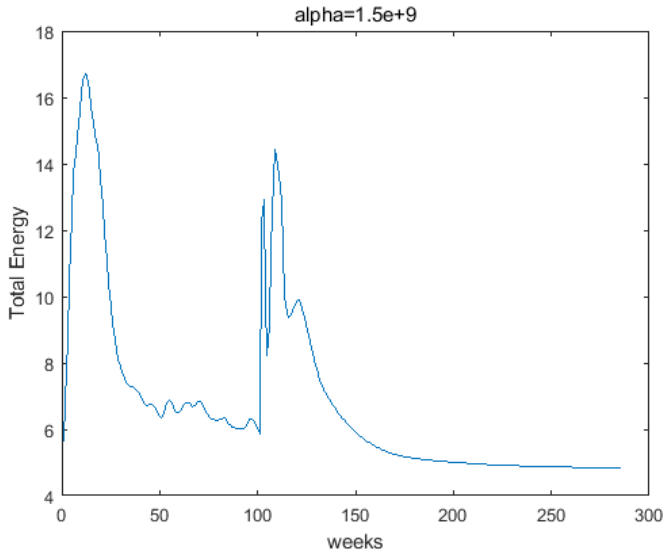

Figure 3.5: The total energy plot of coupled Gmodel run. The coefficient α in equation (2.16) is chosen as 1.5×10^9. The coupled atmosphere is activated after week 100.

of the shallower thermocline depth to the east and hence stronger effect on SST.

The steady state at the end of simulation means that our coupled Gmodel is not able to reproduce the oscillations as in the forced model or as the ENSO cycle in reality (Zhang and Li, 2021). This also suggests that the interaction between the ocean and the atmosphere is underestimated. While we keep increasing the value of α, the coefficient that determines the heating process, we find that this coefficient affects the stability of the model such that when $\alpha \geq 2.0 \times 10^9$, the model will become unstable and the total energy will grow to infinity very soon after the coupled scheme is activated. However we are not able to determine whether it is possible for this

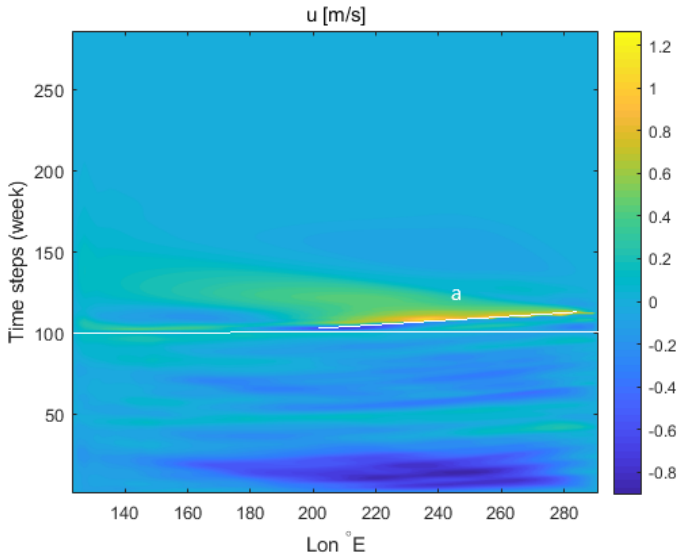

Figure 3.6: Hovmoller diagram of the zonal velocities u averaged in $[0°, 5°N]$ from coupled Gmodel, unit in m/s. Vertical axis indicates the simulated time in weeks, horizontal axis indicates the longitudes. The coupled model is activated after week 100 (shown by white horizontal line). The white line (a) indicates the eastward propagating waves at the beginning of transition, coupled by westward propagating waves with slower zonal velocities characterised by the green "tail" of (a).

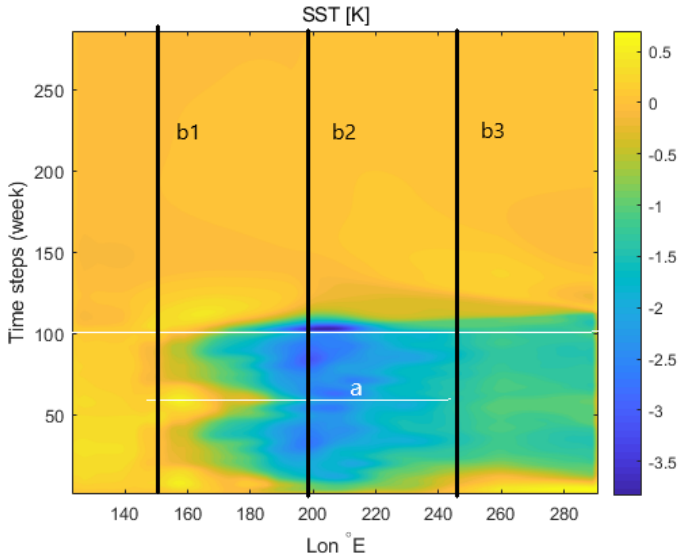

Figure 3.7: Hovmoller diagram of the SST anomalies averaged in $[0°, 5°N]$ from coupled Gmodel, unit in K. Vertical axis indicates the simulated time in weeks, horizontal axis indicates the longitudes. The coupled model is activated at week 100. The white line a indicates the separation of two period in the forced Gmodel before week 100. Black lines $b1$, $b2$, and $b3$ indicate the regions where different coefficients domain in the SST equation.

coupled model to reproduce oscillation behaviours, and what will be the proper

value for α if the oscillations exist.

3.3 ZC model

As discussed in previous sections, the instability waves occur in forced Gmodel while in the coupled Gmodel the system tends to be stable. From the governing equation for atmosphere, we realize that the forcing term is largely determined by SST anomaly, which is determined from equation (2.19). However, the latent heat is not included in the heating force term, and the SST is evaluated through empirical coefficients that need physical explanations. Hence, we choose the ZC model as it contains a more realistic SST model.

The model is initialized with geostrophic currents derived from $H(y)$, while the velocities in the surface mixing layer are assumed to be identical to that in the underlying layer. The result shows that periodical oscillations exist in this model simulation, presented by Fig.3.8. The oscillations have period of around 67 days (200 time steps), shorter than obtained from the forced Gmodel.

The zonal velocities are calculated as $u = (u_1h_1 + u_2h_2)/h$. The results of zonal velocities and SST are shown in Fig.3.9 and Fig.3.10. As is indicated by the green lines in the zonal velocity figure (Fig.3.9a), westward propagating waves with zonal velocities of about -0.4m/s occur in this simulation. Same waves occur in the SST diagram, however, different from the zonal velocity, SST shows the dispersion pattern. The phase speeds vary from 1.35 m/s to 1.69 m/s in SST diagram. One interesting phenomenon in Fig.3.10 is that the SST anomalies are mostly negative over the whole except the limited part at eastern boundary. The similarity in both figures can be explained by the relationship between SST and advection of zonal currents, and that both parameters are forced by the wind stress. The difference in wave speeds may be related to the thermocline depth. As h is smaller at the eastern part, the temperature reacts quickly to the currents, while at the western part, the thermocline layer is thicker and hence the change in temperature is slower. However, the results of SST shows differences with the observation data. The period of 67 days is too short for the SST anomaly to increase as higher as -20 degree and decrease back to zero. The positive SST anomaly does not exist in the result, indicating the cooling process is overestimated in the model. In Fig.3.9b, we find the sharp transition in velocities as waves passing by. The zonal velocity accelerates from -0.03 m/s to -0.28 m/s within only 20 timesteps (around 6.67 days) and changes direction to +0.05 m/s within the same period of time, showing characteristic of solitary waves. Whilst the evolution of SST seems less intense, as is shown by Fig.3.10b, the sharp transition only occurs when the temperature decreases. This may suggest that the feedback process of SST is sensitive to decrease in zonal velocities but less effective to increase in zonal velocities.

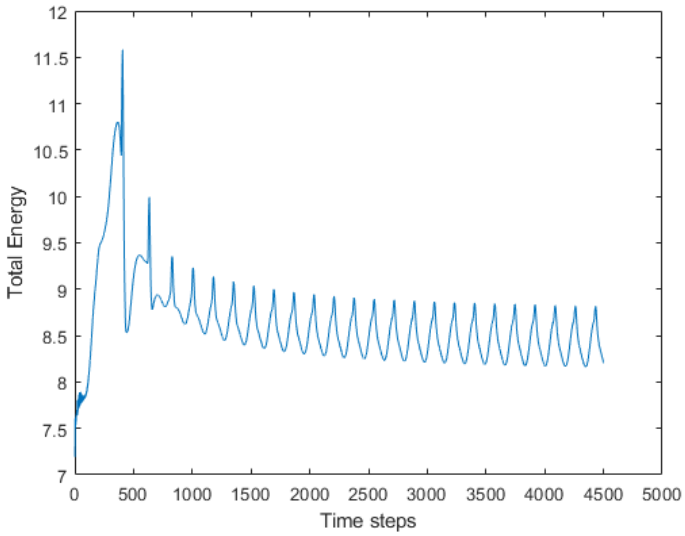

Figure 3.8: Total energy plot of the ZC model. The horizontal axis indicates the time steps of the simulation with unit of 8 hrs. To the end of the simulation, oscillations with period of about 67 days occur.

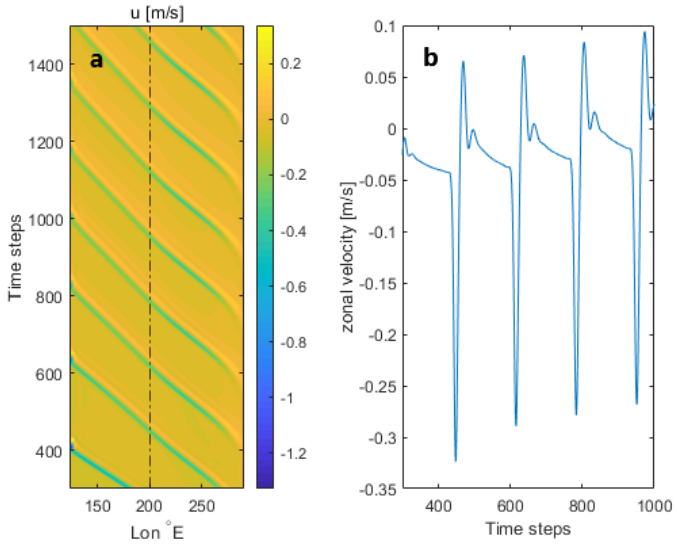

Figure 3.9: (a) Hovmoller diagram of the zonal velocities u averaged in $[0°, 5°N]$ from ZC model, unit in m/s. Vertical axis indicates the simulated time in 8 hrs, horizontal axis indicates the longitudes. The westward propagating waves have phase speed of 1.69 m/s. Dashed line indicates the section at longitude $200°E$. (b) Section plot of Hovmoller diagram (a) at 200 $°E$. The plot shows the evolution of the meridionally averaged zonal velocities from time step 300 to 1000.

3.4 Discussion

The Rossby waves and Kelvin waves are well presented in the first two simulations with Gmodel, though the interaction between atmosphere and the ocean is not in-

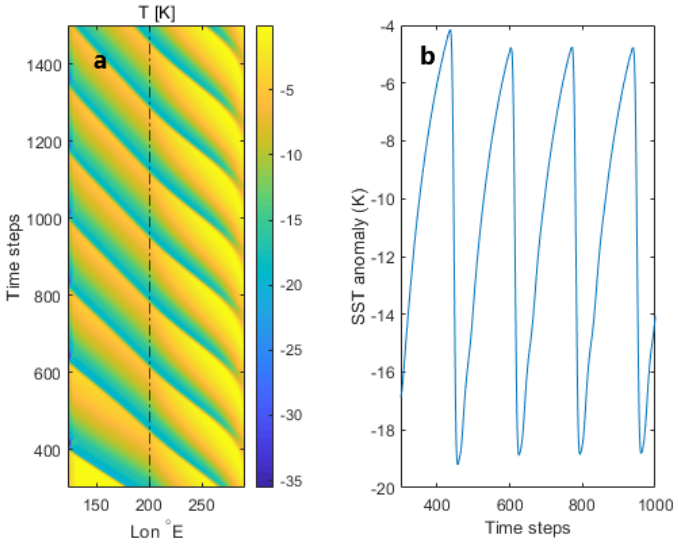

Figure 3.10: (a) Hovmoller diagram of SST anomaly averaged in $[0°, 5°N]$ from ZC model, unit in K. Vertical axis indicates the simulated time in 8 hrs, horizontal axis indicates the longitudes. The westward propagating waves have phase speed of 1.69 m/s. Dashed line indicates the section at longitude $200°E$. (b) Section plot of Hovmoller diagram (a) at 200 $°E$. The plot shows the evolution of the meridionally averaged SST anomaly from time step 300 to 1000.

cluded in the forced model. As is observed in the forced Gmodel, the equatorial Rossby waves and Kelvin waves are generated with the influence of variation in surface wind stresses, which can be view as a form of temporal perturbation, for the reason that the wind stress field is derived from monthly mean values, hence the perturbation occurs with a constant period of one month. However, the Kelvin wave in the forced Gmodel occurs with a frequency of about 2 months on average. One explanation is that the ocean is still developing within the one-month time period of a constant wind force, and whether or not the perturbation in oceanic zonal velocity occurs depend on the structure of the difference in wind fields. Hence, when the zonal difference in wind fields is not strong enough, the Kelvin wave may not occur in the numeric results.

The coupled Gmodel provided an interesting transition from the forced mode to the coupled mode in the beginning, since we can observe the Rossby waves which are generated from the equatorial Kelvin wave. However, the following simulations do not provide robust features about the equatorial instability waves or SST structures under the limitation of the heating rate α discussed in section 3.2.

We do not have a good explanation for the solitary waves shown in the ZC model yet. However, it is reasonable to doubt the heating/cooling process in the model since judging from the results of SST anomaly the equatorial region is dominated by negative SST anomaly which reaches the value of $-19°$C. One possible cause is the extra surface layer included in the ZC model, which is essential to the evolution of the thermocline depth and to the heating/cooling process. In this simulation, the

wind stress only affects the surface layer whose initial value is set to be the same over the whole basin. This may be a good assumption if the meridional spatial scale is small and meridional variation is neglected. However, the meridional variation is considered in our model, and this surface layer needs reconsideration. On the one hand, the surface mixing layer originates from the argument that the Ekman transport only affects limited depth of the ocean, but the Ekman layer lacks definition at the equator: the Ekman layer depth becomes infinity in the classic Ekman theory. Hence it is worthwhile to examine the dynamics at this surface layer. On the other hand, the concept of surface mixing layer is supported by observational data (Dijkstra and Burgers, 2002), it then becomes an interesting subject to find the physical mechanism behind this phenomenon.

Although we observe some features of the ocean currents from the numerical results, they cannot represent the dynamics within the equatorial region because the space resolution in latitude is 1°, which is not sufficient for the equatorial dynamics. Another problem with the numerical models is that both Gmodel and the ZC model are 2D models, so the vertical structure of the ocean currents is not presented. For the purpose of finding a well-defined equatorial surface layer and illustrating the vertical structure of oceanic currents in equatorial region, we apply analytical methods including dimensional analysis and asymptotic expansions, solving the problem in the theoretical perspective.

Chapter 4

Analytical Analysis

4.1 Nontraditional surface Ekman layer

The first problem we intend to solve is how to describe the surface Ekman layer in the equatorial region. The governing equations for the surface layer are:

$$u_t + \tilde{f}w - fv + p_x = A_v u_{zz}, \tag{4.1}$$

$$v_t + fu + p_y = A_v v_{zz}, \tag{4.2}$$

$$w_t - \tilde{f}u = A_v w_{zz}, \tag{4.3}$$

and the boundary conditions are:

$$u_z(z=0) = \frac{\tau^x}{\rho_0 A_v}, \tag{4.4}$$

$$v_z(z=0) = \frac{\tau^y}{\rho_0 A_v}. \tag{4.5}$$

where $f = 2\Omega \sin\phi$ and $\tilde{f} = 2\Omega \cos\phi$ are Coriolis parameters, $\Omega = 7.29 \times 10^{-5} rad/s$ is the magnitude of the Earth's angular velocity, ϕ is the latitude, and A_v is the viscosity coefficient in the vertical direction. Compared to the classical Ekman theory, two nontraditional Coriolis force terms $\tilde{f}w$ and $\tilde{f}u$ are added to the equations. The traditional Coriolis terms (fu and fv) become 0 near the equator ($\phi = 0$), hence $\tilde{f}w$ cannot be neglected in the equation. The typical latitude at which the two Coriolis force terms have the same magnitude ($\tilde{f}w = fv$) is given by:

$$\phi = \frac{W}{V} \approx 0.001 \approx 0.06^\circ, \tag{4.6}$$

where the approximation $\phi = \tan\phi$ is used as ϕ is a small value. This shows that we are actually studying a narrow band region near the equator. To simplify the problem, we set A_v as a constant and do not consider horizontal viscosity. When examining the steady solution as $t \to \infty$, the solution of the above equations is:

$$\begin{pmatrix} u \\ v \\ w \end{pmatrix} = \frac{\sqrt{2}e^{\frac{z}{d}}}{2\rho_0 \Omega d} \begin{pmatrix} \tau^x & \tau^y \csc\phi \\ \tau^y & \tau^x \sin\phi \\ -\tau^y \cot\phi & -\tau^x \cos\phi \end{pmatrix} \begin{pmatrix} \cos(\frac{z}{d} - \frac{\pi}{4}) \\ \sin(\frac{z}{d} - \frac{\pi}{4}) \end{pmatrix} + \begin{pmatrix} 0 \\ w_0 \cot\phi \\ w_0 \end{pmatrix}. \tag{4.7}$$

where $d = \sqrt{\frac{A_v}{\Omega}}$ is the Ekman layer depth, $w_0 = \frac{\tau^y \cot\phi}{2\rho_0 \Omega d} - \frac{\tau^x \cos\phi}{2\rho_0 \Omega d}$ under the assumption of a rigid surface that vertical velocity is zero at $z = 0$. This solution is very similar to that of the classical Ekman theory. The Ekman layer depth is a constant value and does not depend on latitude, which is very different from the classical Ekman theory and can support the existence of an extra surface layer in the ZC model. Vertically, the velocities decay exponentially with depth while an extra term related to w_0 exists even deep in the ocean, which may suggest the occurrence of deep returning currents. In the meridional direction, however, we notice this set of solutions does not solve the singularity at the equator ($\phi = 0$), unless the wind stress field is constrained by:

$$\tau^y(y = 0) = 0, \tag{4.8}$$

$$\lim_{\phi \to 0}(\tau^{y(2)} - 2\tau^{x(1)} \cos\phi) = 0 \tag{4.9}$$

where superscript (2) and (1) represent the second order derivative and the first order derivative to latitude ϕ respectively. This means that meridional wind stress vanishes at the equator, and the zonal stress varies with latitude. Surprisingly, these descriptions of the wind field are expected in reality as the zonal stress becomes stronger approaching the equator with a direction pointing to the west and was used by Constantin and Johnson (2019) to deduce the equtorial Ekman-type solution. However, there is a flaw in logic in that we actually derive constraints for the wind field from the pattern of solution (4.7), while in fact we need to formulate the solution for the surface Ekman layer from an arbitrary wind field structure.

The singularity at the equator indicates that similar rescaling of coordinates is also required at the equator in meridional direction.

4.2 Equatorial boundary layers (BL)

To fix the singularity problem at the equator we need to rescale coordinates and hence regard the equator as a free boundary of the ocean. The governing equations and dimensional magnitudes of the terms are stated as:

$$\begin{array}{cccccc} 2\Omega w & - & \dfrac{2\Omega}{R} yv & = A_v u_{zz} + & A_h u_{yy}, \\ 2\Omega W & \dfrac{2\Omega L_y V}{R} & & \dfrac{A_v U}{D^2} & \dfrac{A_h U}{L_y^2}, \end{array} \tag{4.10}$$

$$\begin{array}{cccccc} \dfrac{2\Omega}{R} yu & & = A_v v_{zz} + A_h v_{yy} & & -p_y, \\ \dfrac{2\Omega L_y U}{R} & & \dfrac{A_v V}{D^2} & \dfrac{A_h V}{L_y^2} & \dfrac{P}{L_y}, \end{array} \tag{4.11}$$

$$\begin{array}{rcccc} -2\Omega u & = & A_v w_{zz} + A_h w_{yy} & -p_z, \\ 2\Omega U & & \frac{A_v W}{D^2} \quad \frac{A_h W}{L_y^2} & \frac{P}{D}, \end{array} \tag{4.12}$$

$$\begin{array}{ccc} v_y + & w_z = 0, \\ \frac{V}{L_y} & \frac{W}{D}, \end{array} \tag{4.13}$$

where R is the radius of the Earth, A_h is the horizontal viscosity coefficient, the dimensions of variables (u, v, w, y, z, p) are (U, V, W, L_y, D, P). We use the beta-plane assumption in these equations and include also the nontraditional Coriolis terms. To rescale these equations, we use following criteria:

1. Divergence terms have the same order. $\frac{V}{L_y} = \frac{W}{D}$.
2. Coriolis force term has same order as perturbation pressure gradient force in vertical momentum equation. $P = 2\Omega U D$.
3. Horizontal and vertical diffusion terms have same orders. $\frac{D}{L_y} = \sqrt{\frac{A_v}{A_h}}$.
4. $U = V$.

The new dimensions are chosen as $D = \frac{A_v}{A_h} R$, $L_y^2 = DR$, $U = V = \frac{L_y}{D} W$. Hence, we obtain the dimensionless equations with scaling $y = L_y \eta$ and $z = D\zeta$:

$$w - \eta v = \epsilon_1 \nabla^2 u, \tag{4.14}$$
$$\eta u = \epsilon_1 \nabla^2 v - p_\eta, \tag{4.15}$$
$$-u = \epsilon_1 \epsilon_2 \nabla^2 w - p_\zeta, \tag{4.16}$$
$$v_\eta + w_\zeta = 0, \tag{4.17}$$

where $\nabla^2 = \partial_{\eta\eta} + \partial_{\zeta\zeta}$, $\epsilon_1 = \frac{A_v}{2\Omega D^2}\sqrt{\frac{A_h}{A_v}}$ and $\epsilon_2 = \frac{A_v}{A_h}$. We notice that $\epsilon_1 = (\frac{d_E}{D})^2 \sqrt{\frac{A_h}{A_v}}$ where $d_E = \sqrt{\frac{A_v}{2\Omega}}$ is the typical magnitude of Ekman layer depth. Under the assumption that Ekman layer is much thinner compared to the water column, $\epsilon_1 << 1$ is treated as a small parameter. Moreover, the viscosity in horizontal direction is much larger than the viscosity in the vertical direction, therefore ϵ_2 is also taken as a small parameter, hence the small order term $\epsilon_1 \epsilon_2 \nabla^2 w$ in equation (4.16) can be neglected and we have:

$$u = p_\zeta. \tag{4.18}$$

By introducing the stream function $v = -\psi_\zeta$, $w = \psi_\eta$ the equations (4.14)-(4.15) are written as:

$$\psi_\eta + \eta \psi_\zeta = \epsilon_1 \nabla^2 p_\zeta, \tag{4.19}$$
$$p_\eta + \eta p_\zeta = -\epsilon_1 \nabla^2 \psi_\zeta, \tag{4.20}$$

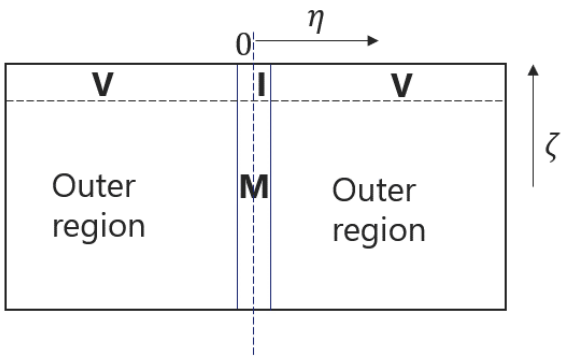

Figure 4.1: Schematic diagram of the separation of regions. **V**: BL in vertical direction, **M**: BL in meridional direction, **I**: BL in the intersection region.

where $u = p_\zeta$ has already been used. Introducing new variable $\varphi = \psi + ip$ ($i^2 = -1$). Combine by adding i(4.20) to (4.19), we obtain:

$$i\epsilon\nabla^2\varphi_\zeta + \varphi_\eta + \eta\varphi_\zeta = 0, \tag{4.21}$$

where $\epsilon = \epsilon_1$ is a small parameter. The equation is difficult to solve or interpret since we have small perturbation terms both in meridional direction and in the vertical direction. Therefore we separate the region into 4 parts (Fig.4.1) and tackle the problem within each part through the asymptotic expansion method, before connecting the solutions together. The outer region is the major part of the equatorial ocean and does not contain any boundary layer. Vertical region **V** and meridional region **M** contain only one boundary layer, and their intersection, region **I**, is treated as two boundary layers.

4.2.1 Outer region

The solution for the outer region is obtained by solving equation (4.21) up to $\mathcal{O}(1)$ in epsilon, which gives us:

$$\varphi_\eta + \eta\varphi_\zeta = 0. \tag{4.22}$$

The solution of this equation has a very simple form:

$$\varphi^O = F(\zeta - \frac{1}{2}\eta^2), \tag{4.23}$$

where superscript O denotes the solution in the outer region, and F is an arbitrary function. Obviously, the outer solution in the equatorial region follows the characteristics consisting of parabolic curves $\zeta - \frac{1}{2}\eta^2 = c$, and the value for φ remains identical along each curve. The value for F is still unknown in the outer region, but it can be obtained by the information in the surface boundary layer, region **V**.

The outer region has no constraints at the equator and does not provide additional information on the equator. But, the outer solution can be separated into the "northern" part F_+, where the solution is solved when $\eta > 0$, and the "southern" part F_-,

when $\eta < 0$. This is possible since the behaviour of the surface boundary layer is determined by the wind stress which is not necessarily symmetric to the equator.

4.2.2 Surface boundary layer (region V)

The surface boundary layer serves the same role as the surface Ekman layer. Actually, after rescaling $Z = \frac{\zeta}{\sqrt{\epsilon}}$ and retaining dominant terms only, we obtain:

$$\partial_Z(i\varphi_{ZZ} + \eta\varphi) = 0, \tag{4.24}$$

which is identical to the equations for the classical Ekman layer:

$$-\eta v = u_{zz}, \tag{4.25}$$

$$\eta u = v_{zz}. \tag{4.26}$$

The boundary condition is $\varphi^V_{\zeta\zeta}(\zeta = 0) = -\tau^y + i\tau^x$, where the superscript V denotes the solution in the vertical boundary layer region. Another constraint on the solution is deduced from the asymptotic method which requires the solution φ^V in the vertical boundary layer **V** as $Z \to -\infty$ to match with the outer solution φ^O as $z \to 0$:

$$\lim_{Z\to-\infty} \varphi^V(\eta, Z) = \varphi^O(\eta, 0) = F(-\frac{1}{2}\eta^2).$$

The solution of (4.24) that satisfies this matching condition in the surface boundary layer, in which η is interpreted as a parameter, is:

$$\varphi^V = \frac{c(\epsilon)}{\eta}\exp(\frac{1+i}{\sqrt{2}}\sqrt{\eta}Z) + F(-\frac{1}{2}\eta^2), \tag{4.27}$$

where $c(\epsilon) = \epsilon(i\tau^y + \tau^x)$, a coefficient depending on the wind stress field and parameter ϵ.

The solution in this region **V** is different from what is obtained in section 4.1: the nontraditional Coriolis terms are neglected in the first step. This is reasonable since we are examining the surface boundary layer only within off-equatorial regions. Hence, the same problem as in the classic Ekman theory still exists that the surface layer depth amplifies up to infinity when approaching the equator. This is expected to be solved in the intersection region **I**.

While the solution for the Ekman layer only gives $\partial_Z\varphi^V$, the outer solution $F(-\frac{1}{2}\eta^2)$ acts as an integration coefficient, which means that the outer solution is determined from the value for φ^V at the surface ($Z = 0$). One can deduce F from surface values of vertical velocity w_0 and meridional pressure gradient $p_{\eta,0}$:

$$F'(-\frac{1}{2}\eta^2) = \frac{-w_0 + \epsilon(\frac{\tau^x_\eta}{\eta} - \frac{\tau^x}{\eta^2})}{\eta} + i\frac{-p_{\eta,0} + \epsilon(\frac{\tau^y_\eta}{\eta} - \frac{\tau^y}{\eta^2})}{\eta}, \tag{4.28}$$

where $F' = \partial_y F$. When the wind field and the surface values for w and p_η are given, an outer function F is generated from the surface layer, though the behaviour in the

region **V** is still dominated by an Ekman-type solution. The outer solution become dominant in the outer region and keeps following the parabolic curves $\zeta - \frac{1}{2}\eta^2$, until the curves meet the equatorail boundary layer in meridional direction.

Equation (4.28) can be rewritten as a first order derivative equation to variable $t = -\frac{1}{2}\eta^2$:

$$F_t = \frac{-w_0 + \epsilon(\frac{\tau^x_\eta}{\sqrt{-2t}} + \frac{\tau^x}{2t})}{2t} + i\frac{-p_\eta + \epsilon(\frac{\tau^y_\eta}{\sqrt{-2t}} + \frac{\tau^y}{2t})}{2t}, \tag{4.29}$$

where w_0, τ^x, τ^y and p_η are considered as known functions. However, we are not able to verify the assumption that w_0 and p_η are prescribed and obtained from other sources, for example from satellite observations. In this equation both upwelling/downwelling and surface pressure gradient are interpreted as additional forcing terms similar to the wind stresses, which is different from the classic Ekman theory where wind stress shapes the upwelling/downwelling.

4.2.3 Boundary layer in the meridional direction (region M)

In the region **M**, we use similar rescaling with $Y = \frac{\eta}{\epsilon}$ and keep only the dominant terms in equation (4.21):

$$i\varphi^M_{Y\zeta} + \varphi^M = f(\zeta), \tag{4.30}$$

where $f(\zeta)$ is an arbitrary function obtained as the integration constant, and can be determined later from the matching condition. The homogeneous solution of this equation has the form:

$$\varphi^{M,H} = \begin{cases} a\exp(\frac{i\zeta}{\mu} + \mu Y), & (Y > 0) \\ b\exp(\frac{i\zeta}{\lambda} + \lambda Y). & (Y < 0) \end{cases}. \tag{4.31}$$

where a, b, μ, λ are constant coefficients and $\mu < 0$, $\lambda > 0$. The matching condition is $\lim_{Y\to\infty}\varphi^M = \varphi^0(0,\zeta)$, which determines the particular solution $\varphi^{M,P} = f(\zeta) = F(\zeta)$. Since any function with the above form satisfies the inner equation (4.30), we may write an infinite series of functions instead, and the parameters become a_n, b_n, μ_n and λ_n. However, as mentioned in section 4.2.1, the outer solution F may have a discontinuity at the equator. A difference of $F_+(\zeta) - F_-(\zeta)$ occurs in the particular solution for region **M** occurs:

$$\varphi^M = \begin{cases} F_+(\zeta) + \sum a_n\exp(\frac{i\zeta}{\mu_n} + \mu_n Y), & (Y > 0) \\ F_-(\zeta) + \sum b_n\exp(\frac{i\zeta}{\lambda_n} + \lambda_n Y), & (Y < 0) \end{cases}. \tag{4.32}$$

Instead of countable terms in the homogeneous solution, we have used an infinite series of functions as this is the only way to satisfy the continuity condition at the equator, and the coefficients are determined by Fourier expansions of the odd extension of $F(\zeta)$ (for both F_+ and F_-):

$$S_\pm(x) = \begin{cases} F_\pm(-x), & x > 0 \\ F_\pm(x), & x \le 0 \end{cases}. \tag{4.33}$$

With a constant period δ, the Fourier expansion of function S is given by:

$$S_-(\zeta) = \sum_{-\infty}^{\infty} c_n \exp(\frac{in\pi}{\delta}\zeta), \tag{4.34}$$

$$S_+(\zeta) = \sum_{-\infty}^{\infty} d_n \exp(\frac{in\pi}{\delta}\zeta), \tag{4.35}$$

where

$$\begin{cases} c_n = \frac{1}{2\delta}\int_{-\delta}^{\delta} S_-(\zeta) e^{\frac{-in\pi}{\delta}\zeta} d\zeta \\ d_n = \frac{1}{2\delta}\int_{-\delta}^{\delta} S_+(\zeta) e^{\frac{-in\pi}{\delta}\zeta} d\zeta \end{cases}.$$

The parameter δ is a constant relating to the typical wave length in vertical direction. For long-waves we can choose it as the total dimensionless depth 1 while for short-waves we can choose it as the dimensionless Ekman layer depth $\frac{d_E}{D}$. Using continuity condition:

$$\lim_{Y\to 0^+} \varphi^M = \lim_{Y\to 0^-} \varphi^M, \tag{4.36}$$

the coefficients $a_n, b_n, \mu_n, \lambda_n$ are calculated as:

$$\begin{cases} a_n = c_{-n} - d_{-n}, \\ b_n = d_n - c_n, \\ \mu_n = \frac{-\delta}{n\pi}, \\ \lambda_n = \frac{\delta}{n\pi}. \end{cases}$$

The above method is developed from mathematical perspective where the odd extension is adapted for the purpose to fix the discontinuity by carrying out the Fourier expansion in equation (4.34) and (4.35), where integration interval extends from $-\delta$ (beneath the ocean surface) to $+\delta$ (in the atmosphere). However, the physical meaning is not well demonstrated as the streamfunction ψ and pressure p do not have definitions in the atmosphere where $\zeta > 0$.

So far, the continuity problem at the equator is solved and the relation of outer region, region **M** and region **V** is established. The pressure gradient, windstress and upwelling (or downwelling) at the ocean surface prescribed the behaviour of ocean currents in the outer region. When the information carried by this outer region solution is transferred within the ocean basin from both northern hemisphere and southern hemisphere, it is conserved along the parabolas. However, at the equator, region **M**, the outer solution produces a discontinuity originating in the difference of surface values in both hemispheres. Hence, the equatorial layer is generated to fulfill the continuity condition and serves as a transient zone for the variation of F_- and F_+. Interestingly, in this interpretation the vertical structure of currents at the equator is related to the meridional structure of currents at the surface as the value at originally horizontally separated curves $-\frac{1}{2}\eta^2 = C$ (C is constant), located at the surface $\zeta = 0$, are identical with the vertically separated curves $\zeta = C$ at $\eta = 0$. Moreover the outer solution F is determined by p_η and windstress induced

upwelling (or downwelling) as discussed in previous section. However, the extent of the meridional structure around the equator is limited. Beyond the separatrix, at which the parabola touches the equatorial bottom, the outer solution follows a particular parabola curve that reaches the bottom of the ocean before reaching the equator. The maximum range where meridional structure participates can be determined by $-\frac{1}{2}(\frac{y}{L_y})^2 = -1$, or $y = \sqrt{2DR}$.

4.2.4 Intersection region (region I)

For the last part of the problem, we investigate the intersection region of the two boundary layers. As has been discussed before, the singularity problem of the surface layer at the equator is only solvable if we consider boundary layers in both vertical and meridional directions. This is achieved via rescaling $Y = \frac{\eta}{\sqrt{\epsilon}}$ and $Z = \frac{\zeta}{\sqrt{\epsilon}}$. We can rewrite equation (4.21) as:

$$\nabla^2 \varphi_Z - i\varphi_Y - i\sqrt{\epsilon} Y \varphi_Z = 0. \tag{4.37}$$

This equation is solvable with a solution:

$$\varphi^I(Y,Z) = \begin{cases} (c_1 Ai(\alpha Y) + c_2 Bi(\alpha Y)) \exp(\frac{i}{2\mu} Y + \mu Z), & Y > 0 \\ -(\bar{c_1} Ai(\alpha Y) + \bar{c_2} Bi(\alpha Y)) \exp(\frac{i}{2\bar{\mu}} Y + \bar{\mu} Z), & Y < 0 \end{cases} \tag{4.38}$$

where the over-lines denote the complex conjugate of the variables, $\alpha = -i\epsilon^{\frac{1}{6}}$, $\mu = \frac{\sqrt{2}}{4}(1-i)$, c_1 and c_2 are undetermined coefficients, $Ai(x)$ and $Bi(x)$ are Airy functions. When we consider the continuity condition at the equator:

$$\lim_{Y \to 0^+} \varphi^I = \lim_{Y \to 0^-} \varphi^I, \tag{4.39}$$

we will get a constraint for c_1 and c_2:

$$\sqrt{3} c_2 + c_1 = 0. \tag{4.40}$$

We have utilized all the constraints on the intersection region, but still the explicit values for c_1 and c_2 are not determined. On the other hand, when the last term in equation (4.37) is considered as a smaller order term, and simplify the equation as:

$$\nabla^2 \varphi_Z - i\varphi_Y = 0, \tag{4.41}$$

the problem of insufficient constraints still exists. By separating variables we can write the solution in intersection region as:

$$\varphi^I(Y,Z) = C_0 \exp(\beta Y + \gamma Z), \tag{4.42}$$

where $\gamma\beta^2 - i\beta + \gamma^3 = 0$ is required but none explicit value can be derived from this relation.

Moreover, using the properties of the Airy function, if we consider the condition:

$$\lim_{Y\to 0^+} \frac{\partial \varphi^I}{\partial Y} = \lim_{Y\to 0^-} \frac{\partial_Y \varphi^I}{\partial Y}, \tag{4.43}$$

which gives a different constraint for c_1 and c_2:

$$\sqrt{3}c_2 - c_1 = 0. \tag{4.44}$$

Equation (4.40) and (4.44) indicate that the only solution that satisfies the two continuity conditions is a trivial solution $\varphi^I = 0$. This means that if nontrivial solution exists at the intersection region, or the ocean is not motionless at the intersection boundary layer, either the solution is not continuous or it is not differentiable (in meridional direction) at the equator.

In both cases (equation 4.38 and 4.42), we need an extra constraint, either from surface evaluation at the equator or from the vertical structure at the equator, to determine remaining parameters. In the first case, both Airy functions contain an exponentially increasing part and an oscillating part in the real domain, however αY is an imaginary number and it remains unclear what the physical meaning of the Airy function in the complex domain is. Hence, it remains a question how to relate the intersection region solution with the two boundary layers **M** and **V** to solve the singularity problem as $\eta \to 0$ and $\zeta \to 0$ simultaneously.

Chapter 5

Conclusion and Outlook

To study the observed SST structure and the behaviour of ocean currents in the equatorial region, we carried out numerical simulations with different set-ups. The results of these simulations illustrate that both Rossby waves and Kelvin waves are generated in the equatorial region under realistic windstresses (forced Gmodel). However, the SST structure is not clearly shown by the model results. The fully coupled model (coupled Gmodel) does not function well judging from the results, and the underestimated air-sea interaction indicated by the steady state at the end of the simulation needs further investigation. The result of Zebiak and Canes's (1987) model shows abnormal nonlinear waves both in zonal velocities and in SST, but the reason behind this phenomenon is not clear. Overall, the numerical models do not provide much information on the equatorial currents or the background SST distribution as we expected, hence we cannot draw any conclusion from the numerical perspective about the role that the equatorial boundary layer is playing in the dynamics in this region. A numeric model with better defined surface layer and boundary conditions may provide more information, though a 3D model is required to study the effects of equatorial boundary layers on the vertical currents structure.

On the other hand, we find that the surface boundary layer introduced in the ZC model deserves more detailed study owing to the limitation in the classic Ekman theory, and we realise that this problem is also related to the existence of a boundary layer in meridional direction near the equator, because a singularity exists at the equator in the solution of current velocities in the classic surface Ekman layer.

Via dimensional analysis and asymptotic methods, we found that the meridional equatorial boundary layer serves as a transition zone that connects both hemispheres and the surface boundary layer directly shapes the currents structure in the ocean domain outside the boundary layers. We also constructed a scheme that potentially connects a free equatorial vertical boundary layer, the off-equatorial surface boundary layer and the atmosphere. The windstresses, upwelling/downwelling along with meridional pressure gradient in the surface boundary layer generates the ocean currents that distribute in the major part (outside of the boundary layers) of the ocean. These ocean currents then produce the meridional boundary layer located near the equator over a limited range in latitude. This scheme may explain the existence of

equatorial deep jets. However, the impact of surface boundary layer on the outer region current structure needs further investigation via comparing the observed equatorial currents structures with that computed from the observational data of meridional surface pressure gradient and vertical velocities using the analytical model we constructed. The analysis of the boundary layer in the meridional direction is not finished either. Although the discontinuity of the solution at the equator is removed via Fourier expansions and function extension, we cannot explain the physical meaning of the extended function (of pressure and velocities) that is defined above in the atmosphere, and the singularity of the solution still exists because discontinuity occurs in the first order gradient (in meridional direction).

We also found some results in the intersection region where the surface boundary layer and the equatorial boundary layer overlap. However, the problem is not closed yet as the discontinuity at the equator still exists and the solution in this region is not completed because the constraints are not sufficient, indicating that some physical processes in this region remain uncovered. Hence, how to solve the singularity problem at the intersection region is still an interesting question for future researches either from a mathematical perspective to complete the asymptotic expansion method or from a physical perspective to discover the overlooked processes that play a governing role in this region.

References

Ascani, F., Firing, E., Dutrieux, P., Mccreary, J. P., and Ishida, A. (2010). Deep equatorial ocean circulation induced by a forced–dissipated yanai beam. *Journal of Physical Oceanography*, 40(5):1118–1142. pages 3

Beckers, J.-M. and Deleersnijder, E. (1993). Stability of a FBTCS scheme applied to the propagation of shallow-water inertia-gravity waves on various space grids. *Journal of Computational Physics*, 108(1):95–104. pages 10

Boulanger, J.-P. (2001). The trident pacific model. part 1: simulating surface ocean currents with a linear model during the 1993-1998 TOPEX/POSEIDON period. *Climate Dynamics*, 17(2-3):159–173. pages 5

Burgers, G. and van Oldenborgh, G. J. (2003). On the impact of local feedbacks in the central pacific on the ENSO cycle. *Journal of Climate*, 16(14):2396–2407. pages 5, 7

Caltabiano, A. C. V., Robinson, I. S., and Pezzi, L. P. (2005). Multi-year satellite observations of instability waves in the tropical atlantic ocean. *Ocean Science*, 1(2):97–112. pages 1

Chu, P. C. and Fan, C. (2019). Global ocean synoptic thermocline gradient, isothermal-layer depth, and other upper ocean parameters. *Scientific Data*, 6(1). pages 8

Constantin, A. and Johnson, R. S. (2019). Ekman-type solutions for shallow-water flows on a rotating sphere: A new perspective on a classical problem. *Physics of Fluids*, 31(2):021401. pages 23

Dijkstra, H. A. and Burgers, G. (2002). Fluid dynamics of El Niño variability. *Annual Review of Fluid Mechanics*, 34(1):531–558. pages 21

Eden, C. and Dengler, M. (2008). Stacked jets in the deep equatorial atlantic ocean. *Journal of Geophysical Research: Planets*, 113(C4). pages 1

Ekman, V. W. (1905). On the influence of the earth's rotation on ocean currents. *Arkiv for Matematik, Astronomi och Fysik*, 2(10):1–52. pages 2

Gill, A. E. (1980). Some simple solutions for heat-induced tropical circulation. *Quarterly Journal of the Royal Meteorological Society*, 106(449):447–462. pages 6

Greatbatch, R. J., Brandt, P., Claus, M., Didwischus, S.-H., and Fu, Y. (2012). On the width of the equatorial deep jets. *Journal of Physical Oceanography*, 42(10):1729–1740. pages 2

Holmes, R. M., Mcgregor, S., Santoso, A., and England, M. H. (2019). Contribution of tropical instability waves to ENSO irregularity. *Climate Dynamics*, 52(3-4):1837–1855. pages 1

Imada, Y. and Kimoto, M. (2012). Parameterization of tropical instability waves and examination of their impact on ENSO characteristics. *Journal of Climate*, 25(13):4568–4581. pages 1

Menkes, C. E. R., Vialard, J. G., Kennan, S. C., Boulanger, J.-P., and Madec, G. V. (2006). A modeling study of the impact of tropical instability waves on the heat budget of the eastern equatorial pacific. *Journal of Physical Oceanography*, 36(5):847–865. pages 1

Tian, F., Zhang, R., and Wang, X. (2019). A positive feedback onto ENSO due to tropical instability wave (TIW)-induced chlorophyll effects in the pacific. *Geophysical Research Letters*, 46(2):889–897. pages 1

Timmermann, A., Oberhuber, J., Bacher, A., Esch, M., Latif, M., and Roeckner, E. (1999). Increased El Niño frequency in a climate model forced by future greenhouse warming. *Nature*, 398(6729):694–697. pages 1

Wei, Y., Pei, Y., and Kang, X. (2019). Assessing feedback of tropical instability wave-induced wind stress perturbations in the equatorial pacific. *International Journal of Climatology*, 39(3):1634–1643. pages 1

Willett, C. S., Leben, R. R., and Lavín, M. F. (2006). Eddies and tropical instability waves in the eastern tropical pacific: A review. *Progress in Oceanography*, 69(2-4):218–238. pages 1, 2

Zebiak, S. E. and Cane, M. A. (1987). A model El Niño–Southern Oscillation. *Monthly Weather Review*, 115(10):2262 – 2278. pages 4

Zhang, Z. and Li, G. (2021). Time-spatial features of mix El Niño. *Atmosphere*, 12(4):476. pages 16

Appendix A

Discretized governing equations

In following equations, superscripts with t indicate the time step of the variables, subscripts with (i, j) indicate the value is evaluated at grid point (i, j).

$$s = \begin{cases} 0 & t = 2k \\ 1 & t = 2k+1 \end{cases}, k \in \mathbf{N},$$

is a counter to decide the sequence of iterations. The variables with a overline are averaged values at corresponding grid point:

$$\bar{u}_{(i+l_1,j+l_2)} = \begin{cases} \frac{1}{2}(u_{(i+\frac{1}{2},j)} + u_{(i-\frac{1}{2},j)}) & l_1 = 0, l_2 = 0 \\ \frac{1}{2}(u_{(i+\frac{1}{2},j)} + u_{(i+\frac{1}{2},j+1)}) & l_1 = \frac{1}{2}, l_2 = \frac{1}{2} \\ \frac{1}{4}(u_{(i+\frac{1}{2},j)} + u_{(i+\frac{1}{2},j+1)} + u_{(i-\frac{1}{2},j)} + u_{(i-\frac{1}{2},j+1)}) & l_1 = 0, l_2 = \frac{1}{2} \end{cases},$$

$$\bar{v}_{(i+l_1,j+l_2)} = \begin{cases} \frac{1}{2}(v_{(i,j+\frac{1}{2})} + v_{(i,j-\frac{1}{2})}) & l_1 = 0, l_2 = 0 \\ \frac{1}{2}(v_{(i,j+\frac{1}{2})} + v_{(i+1,j+\frac{1}{2})}) & l_1 = \frac{1}{2}, l_2 = \frac{1}{2} \\ \frac{1}{4}(v_{(i,j+\frac{1}{2})} + v_{(i+1,j+\frac{1}{2})} + v_{(i,j-\frac{1}{2})} + v_{(i+1,j-\frac{1}{2})}) & l_1 = \frac{1}{2}, l_2 = 0 \end{cases},$$

and

$$\bar{h}_{(i+l_1,j+l_2)} = \begin{cases} \frac{1}{2}(h_{(i,j+1)} + h_{(i,j)}) & l_1 = 0, l_2 = \frac{1}{2} \\ \frac{1}{2}(h_{(i,j)} + h_{(i+1,j)}) & l_1 = \frac{1}{2}, l_2 = 0 \\ \frac{1}{4}(h_{(i,j)} + h_{(i+1,j)} + h_{(i,j+1)} + h_{(i+1,j+1)}) & l_1 = \frac{1}{2}, l_2 = \frac{1}{2} \end{cases}.$$

The governing equations for the mixing layer are:

$$\begin{aligned} &\frac{h^{t+1}_{1,(i,j)} - h^t_{1,(i,j)}}{\Delta t} \\ &+ \frac{(u^t_{1,(i+\frac{1}{2},j)} + u^t_{1,(i+\frac{3}{2},j)})h^t_{1,(i+1,j)} - (u^t_{1,(i-\frac{1}{2},j)} + u^t_{1,(i-\frac{3}{2},j)})h^t_{1,(i-1,j)}}{4\Delta x} \\ &+ \frac{(v^t_{1,(i,j+\frac{1}{2})} + v^t_{1,(i,j+\frac{3}{2})})h^t_{1,(i,j+1)} - (v^t_{1,(i,j-\frac{1}{2})} + v^t_{1,(i,j-\frac{3}{2})})h^t_{1,(i,j-1)}}{4\Delta y} = 0, \end{aligned} \tag{A.1}$$

$$\frac{u^{t+1}_{1,(i+\frac{1}{2},j)} - u^{t}_{1,(i+\frac{1}{2},j)}}{\Delta t} - \beta_0 y_j \overline{v}^{t+s}_{1,(i+\frac{1}{2},j)} = -g' \frac{h^{t+1}_{(i+1,j)} - h^{t+1}_{(i,j)}}{\Delta x} + \frac{\tau^{x,t}_{(i+\frac{1}{2},j)}}{\rho \bar{h}^{t}_{(i+\frac{1}{2},j)}} + DA_u, \quad \text{(A.2)}$$

$$\frac{v^{t+1}_{1,(i,j+\frac{1}{2})} - v^{t}_{1,(i,j+\frac{1}{2})}}{\Delta t} + \beta_0 \overline{y}_{j+\frac{1}{2}} \overline{u}^{t+1-s}_{1,(i,j+\frac{1}{2})} = -g' \frac{h^{t+1}_{(i,j+1)} - h^{t+1}_{(i,j)}}{\Delta y} + \frac{\tau^{y,t}_{(i,j+\frac{1}{2})}}{\rho \bar{h}^{t}_{(i,j+\frac{1}{2})}} + DA_v. \quad \text{(A.3)}$$

The governing equations for the underlying layer are:

$$\begin{aligned} &\frac{h^{t+1}_{2,(i,j)} - h^{t}_{2,(i,j)}}{\Delta t} \\ &+ \frac{(u^{t}_{2,(i+\frac{1}{2},j)} + u^{t}_{2,(i+\frac{3}{2},j)}) h^{t}_{2,(i+1,j)} - (u^{t}_{2,(i-\frac{1}{2},j)} + u^{t}_{2,(i-\frac{3}{2},j)}) h^{t}_{2,(i-1,j)}}{4\Delta x} \\ &+ \frac{(v^{t}_{2,(i,j+\frac{1}{2})} + v^{t}_{2,(i,j+\frac{3}{2})}) h^{t}_{2,(i,j+1)} - (v^{t}_{2,(i,j-\frac{1}{2})} + v^{t}_{2,(i,j-\frac{3}{2})}) h^{t}_{2,(i,j-1)}}{4\Delta y} = 0, \end{aligned} \quad \text{(A.4)}$$

$$\frac{u^{t+1}_{2,(i+\frac{1}{2},j)} - u^{t}_{2,(i+\frac{1}{2},j)}}{\Delta t} - \beta_0 y_j \overline{v}^{t+s}_{2,(i+\frac{1}{2},j)} = -g' \frac{h^{t+1}_{(i+1,j)} - h^{t+1}_{(i,j)}}{\Delta x} + DA_u, \quad \text{(A.5)}$$

$$\frac{v^{t+1}_{2,(i,j+\frac{1}{2})} - v^{t}_{2,(i,j+\frac{1}{2})}}{\Delta t} + \beta_0 \overline{y}_{j+\frac{1}{2}} \overline{u}^{t+1-s}_{2,(i,j+\frac{1}{2})} = -g' \frac{h^{t+1}_{(i,j+1)} - h^{t+1}_{(i,j)}}{\Delta y} + DA_v, \quad \text{(A.6)}$$

For dynamic atmosphere model, we have similar equations as for the underlying layer by replacing h_2 with p, and replacing (u_2, v_2) with (u, v). However, for the slow heating rate situation which is used in the coupled Gmodel, the time derivative in equations does not exist, hence we calculate the equations using one equation for pressure in the form:

$$\frac{-\epsilon}{\epsilon^2 + \frac{1}{4}y^2} p_{yy} + \frac{\frac{1}{2}\epsilon y}{(\epsilon^2 + \frac{1}{4}y^2)^2} p_y - \frac{\epsilon}{\epsilon^2 + \frac{1}{4}y^2} p_{xx} - \frac{\frac{1}{2}\epsilon^2 - \frac{1}{8}y^2}{(\epsilon^2 + \frac{1}{4}y^2)^2} p_x + \epsilon p = -Q. \quad \text{(A.7)}$$

The above equation is derived from the Gill's atmosphere governing equations and is used in the following numerical calculations. Note that the equation is already reduced to dimensionless version by the length scale $(\frac{c_a}{2\beta_0})^{0.5}$, and the time scale $(2\beta_0 c_a)^{-0.5}$.

The derivatives are descretized as:

$$\begin{aligned} p_{yy} &= \frac{1}{(\Delta y)^2}(p_{(i,j+1)} + p_{(i,j-1)} - 2p_{(i,j)}), \\ p_y &= \frac{1}{2\Delta y}(p_{(i,j+1)} - p_{(i,j-1)}), \\ p_{xx} &= \frac{1}{(\Delta x)^2}(p_{(i+1,j)} + p_{(i-1,j)} - 2p_{(i,j)}), \\ p_x &= \frac{1}{2\Delta x}(p_{(i+1,j)} - p_{(i-1,j)}), \end{aligned}$$

$$p_{xy} = \frac{1}{4\Delta x \Delta y}(p_{(i+1,j+1)} + p_{(i-1,j-1)} - p_{(i-1,j+1)} - p_{(i+1,j-1)}).$$

Then, equation (A.7) is descretized as:

$$\begin{aligned}(\epsilon - \frac{2A_3}{\Delta x^2} - \frac{2A_1}{\Delta y^2})p_{(i,j)} + (\frac{A_4}{2\Delta x} + \frac{A_3}{\Delta x^2})p_{(i+1,j)} + (\frac{A_3}{\Delta x^2} - \frac{A_4}{2\Delta x})p_{(i-1,j)} \\ +(\frac{A_1}{\Delta y^2} + \frac{A_2}{2\Delta y})p_{(i,j+1)} + (\frac{A_1}{\Delta y^2} - \frac{A_2}{2\Delta y})p_{(i,j-1)} = -Q_{(i,j)},\end{aligned} \tag{A.8}$$

with:

$$\begin{aligned}A_1 &= \frac{-\epsilon}{\epsilon^2 + \frac{1}{4}y^2}, \\ A_2 &= \frac{\frac{1}{2}\epsilon y}{(\epsilon^2 + \frac{1}{4}y^2)^2}, \\ A_3 &= -\frac{\epsilon}{\epsilon^2 + \frac{1}{4}y^2}, \\ A_4 &= \frac{\frac{1}{2}\epsilon^2 - \frac{1}{8}y^2}{(\epsilon^2 + \frac{1}{4}y^2)^2}.\end{aligned}$$

The solution of this equation is calculated by finding the inverse of the 5160×5160 ($86 \times 60 = 5160$ elements per column/row) coefficient matrix using LAPACK.